THERMAL STATE EVOLUTION AND THERMAL SUPPRESSION BEHAVIOR IN THE INSULATION SPACE OF HELIUM WORKER DRIVE MOTORS FOR HIGH TEMPERATURE GAS-COOLED REACTORS

Xiao Xu[1], Shengnan Li*[1], Jingyu Bu[2], Yidong Wang[1], Wanyi Zhang[1], Yu Zhou[3]

[1]School of Electrical and Electronic Engineering, Harbin University of Science and Technology, Harbin 150080, Heilongjiang Province, China.

[2]Harbin Electric Group Jiamusi Electric Motor Co., Ltd, Jiamusi 154000, Heilongjiang Province, China.

[3]North China Branch of State Grid Corporation of China, Beijing 100053, China

[*] Corresponding author: E-mail: 2220310095@stu.hrbust.edu.cn.

Abstract—The insulation space designed to mitigate the effects of a high-temperature gradient environment in high-temperature gas-cooled reactors is crucial for the normal operation of drive motors. This paper explores the insulation space's thermal suppression characteristics and dominant factors by employing the field and circuit combination method to simulate the fluid-thermal evolution. It reveals the heat transfer modes and elucidates the mechanisms underlying thermal suppression behavior, enhancing model accuracy through experimental data integration. A thermal equilibrium assessment method is introduced, which constructs the spatial relationship of temperature parameters and the nonlinear mapping between environmental variables, structural parameters, and judgment criteria. Additionally, the response surface method is utilized to optimize the through-hole structure of the insulation space. Findings indicate that thermal convection primarily inhibits heat transfer within the insulation space in high-temperature gradient environments; both pressure and through-hole structure significantly influence the thermal state distribution characteristics. After optimizing the nonlinear structural parameters, the thermal balance performance of the insulation space was improved by 9.12% compared to the original model when the number of holes was 7 and the diameter was 66 mm, and the vortex situation in the insulation space watershed was effectively improved. This paper offers a foundational research basis and novel insights for the heat exchange system of high -temperature gas-cooled reactors, with broader implications for high -temperature motor system studies.

Key words*: heat transfer method, insulated space, response surface optimization, thermal simulation, thermal equilibrium.*

1. Introduction

Amid global resource constraints and escalating environmental pollution issues [1, 2], the development of nuclear energy is becoming increasingly critical. High-temperature gas-cooled reactors (HTGRs) represent the pinnacle of the Generation IV nuclear power systems. They have emerged as focal points in global nuclear power development due to their excellent safety features, high efficiency, and versatility [3]. The main helium fan of the high-temperature gas-cooled reactor includes two chambers. The drive motor's temperature in the working chamber is maintained below 65°C by a heat exchange system, while the internal helium temperature in the fan chamber can rise to at least 250°C during normal operation due to circuit heat [4]. Under high-temperature gradients, in order to reduce the impact of high-temperature helium gas in the first loop of the reactor on the working chamber of the drive motor, the insulation space plays an important role in isolating external heat source interference and suppressing helium gas reflux on the first loop side. The schematic diagram of the working chamber and insulation space is shown in Figure 1. As the largest barrier to maintaining the stability of the working chamber environment, clarifying the heat transfer law and key factors of thermal suppression behavior in the insulation space and proposing targeted structural optimization strategies are of great significance for improving the long-term service capability of the drive motor and achieving the large-scale development of high-temperature gas-cooled reactors.

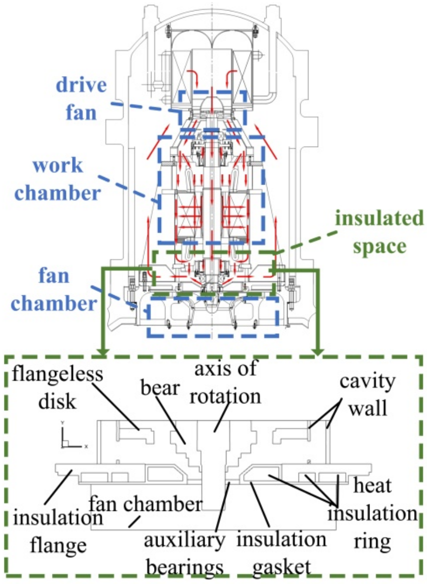

Fig. 1. Sketch of working chamber and insulated space.

Given that high-temperature gas-cooled reactors are still in the research and demonstration stage, their core technologies (such as fuel manufacturing, helium circulation, high-temperature suppression, etc.) are not fully mature, and scientific research progress is still in the early stages of laboratory or prototype reactor exploration. There has been no relevant research on insulation space at home and abroad, and only engineer Zou Debao from China Jiamusi Electric Power Plant has briefly summarized their structural functions [4]. Conducting research on heat transfer in multi-temperature zone cavity structures for thermal insulation space, establishing a flow resistance network for the research target using fluid network method and calculating the flow parameters at each node can serve as the basis for further solving related heat transfer problems [5-7]. Some studies have shown that there is an interaction between surface heat radiation and natural convection heat transfer in the cavity body under different conditions, and the influence of heat radiation on the temperature field of the cavity cannot be ignored [8-13]. Therefore, exploring the dominant heat transfer mode of each component in the thermal evolution process of the thermal insulation space is a necessary step to reveal the causes of its thermal suppression behavior. Non-steady-state numerical simulation of the cooling effect of a stationary heating element under strong convective heat transfer considering various factors such as temperature and pressure [14]. A series of academic achievements, such as the establishment and simulation calculation of a coupled heat transfer model with a built-in surface heat source in a closed square cavity [15, 16], can demonstrate that clarifying the influencing factors and variation laws of flow heat parameters in space is an important core for highlighting the theoretical research value of gradient temperature difference control.

At the same time, as a key structure in the "insulation space", if the insulation flange is in an environment with high-temperature gradient, if the temperature distribution of the structure is uneven, the internal thermal expansion deformation will cause uneven anisotropic thermal stress, which may cause local structural damage. The uniformity of its thermal distribution also needs to be carefully considered [17-20]. For the analysis of uniformity, most articles only analyze it through data and cloud maps [21-25]. Therefore, in order to further effectively study and improve the thermal uniformity distribution of key structures in thermal insulation spaces, it is necessary to propose a thermal parameter evaluation method that can intuitively analyze thermal balance. In summary, a closed-loop theoretical research route has been formed for simulating the thermal distribution of insulation spaces, analyzing heat transfer mechanisms, and optimizing functional enhancement. Furthermore, a spatial gradient temperature difference suppression strategy has been proposed, which can not only fill the research gap in the overall heat transfer mechanism of drive motors but also achieve a new goal of enhancing the robust service capability of motors and their systems.

This article aims to explore the causes of thermal suppression in thermal insulation spaces and improve their structural functionality. It comprehensively describes the heat transfer process in the thermal insulation space of drive motors under high temperature gradients, fully based on the actual cavity structure of the thermal insulation space. A fluid network topology and multi-field coupling calculation model are established to simulate the thermal evolution of the thermal insulation space under high temperature gradients. By determining the key structural roles and related influencing factors in the thermal suppression behavior of the space, the nonlinear mapping relationship between the variable structural parameters of the space wall and the thermal evaluation parameters is revealed, and targeted optimization strategies for the space structure are proposed. This provides theoretical support for improving the long-term service capacity of the drive motor and its system, enhancing the safety and reliability of the reactor.

This paper not only provides a technical reference for enhancing the service capabilities of helium-driven motors in high-temperature gas-cooled reactors but also offers a theoretical foundation for designing special motors capable of operating under high-temperature gradients, using the thermal parameter judgment method discussed herein.

2. Insulated space modeling and calculations

2.1. Modeling and calculation of fluid networks in insulated spaces

To derive the relevant boundary conditions for three-dimensional fluid-heat coupling calculations, the fluid network method is employed to solve for the flow paths within the heat-insulating space. This approach relies on hypotheses and computational principles related to fluid networks, including flow rate, pressure drop, and loss calculation formulas for flow path nodes, as referenced in [5-7].

The calculation of equivalent wind resistance in the fluid network is determined by solving for the equivalent wind resistance, as given-in Eq. (1):

$$Z = \frac{\rho\zeta}{2A^2} \tag{1}$$

where ζ denotes the drag coefficient; ρ is the density of the medium in the flow path, in $\mathrm{kg/m^3}$; A is the area of the characteristic cross-section of the flow path, in $\mathrm{m^2}$; Z represents the wind resistance of each branch.

The fluid network method involves solving matrix Eq. (2) through network topology theory:

$$\begin{bmatrix} A & 0 \\ -Q & A^T \end{bmatrix} \begin{bmatrix} Q \\ H \end{bmatrix} = \begin{bmatrix} Q_S \\ C \end{bmatrix} \tag{2}$$

where A is the node-branch association matrix; Q is the branch flow column vector; Q_S is the node source flow column vector; H is the node pressure column vector; D and C are constant matrices. The matrix is initially populated with Q_S and subsequently used to solve for Q and H. The velocity-is calculated using the flow rate and the cross-sectional area.

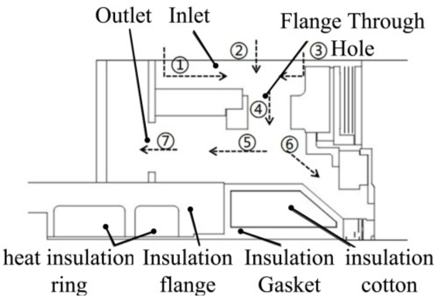

Fig. 1. Insulated space flow path numbering diagram.

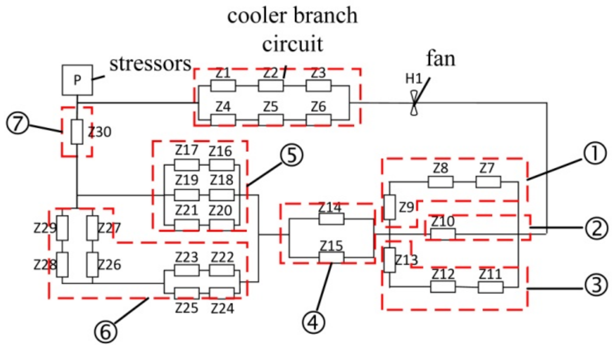

Fig. 2. Insulated space fluid network modeling.

Tab. 1 Calculation results of equivalent flow path.

Number	Position	Equivalent Flow Resistance($\mathrm{N{\cdot}s^2/m^8}$)	Equivalent cross-sectional area($\mathrm{m^2}$)	Volume Flow Rate($\mathrm{m^3/s}$)	Reynolds number at branch inflow node
①-③	Inlet	1.124	1.15	11.80	50806.03(Z10)
④	Flange Through Hole	2.523	0.08	11.80	512688.30(Z18)
⑤	Through-hole outlet flow path 1	0.206	0.17	10.06	227861.47(Z14)
⑥	Through-hole outlet flow path 2	0.825	0.10	1.74	162758.19(Z22)
⑦	Outlet	2.183	0.11	11.73	274288.82(Z30)

Fig. 2 shows the structure of the heat-insulating space and the fluid flow direction with the main wind paths and structural components labeled. Fig. 3 illustrates the fluid network model, where each flow path in the cavity is represented by equivalent wind resistance through series-parallel connections. The helium gas in the main helium fan is driven and circulated by the fan above the driving motor, with the working chamber of the motor being a sealed structure. The inlet flow rate of the insulated space is equivalent to the air volume of the driving fan (H1). The fan has a diameter of 1060 mm and rotates in sync with the motor at a speed of 1494 rad/min.
Tab. 1 shows the results of equivalent wind resistance and flow rate calculations for each branch and the Reynolds number at the main nodes. The total inlet helium flow rate is $11.80\mathrm{m}^3/\mathrm{s}$, which provides boundary conditions for thermal simulation of insulated spaces.

2.2. Mathematical and physical modeling of insulated spaces

The fluid within the cavity exhibits turbulent flow, modeled using the widely accepted standard $k-\varepsilon$ model for simulating turbulence. The transport equations for turbulent kinetic energy k and the dissipation rate ε are specified in Eq. (3). Fluid flow and heat transfer in an insulated space adhere to the laws of conservation of mass, momentum, and energy, as demonstrated in Eq. (4).

$$\begin{cases} \dfrac{\partial(\rho k)}{\partial t}+\mathrm{div}(\rho k\boldsymbol{V})=\mathrm{div}\left[\left(\mu+\dfrac{\mu_t}{\sigma_k}\right)\mathrm{grad}k\right]+G_k-\rho\varepsilon \\ \dfrac{\partial(\rho\varepsilon)}{\partial t}+\mathrm{div}(\rho\boldsymbol{V}\varepsilon)=\mathrm{div}\left[\left(\mu+\dfrac{\mu_t}{\sigma_\varepsilon}\right)\mathrm{grad}\varepsilon\right]+C_{1\varepsilon}G_k\varepsilon/k-C_{2\varepsilon}\rho\varepsilon^2/\mathrm{k} \end{cases} \tag{3}$$

where ρ is the fluid density (kg/m^3); $\boldsymbol{V}$ is the fluid velocity vector (m/s); t is the time (s); $\mathrm{G_k}$ is the turbulence generation rate; μ_t is the turbulence viscosity coefficient; $C_{1\varepsilon}$ and $C_{2\varepsilon}$ are constants; and σ_k and σ_ε are the turbulence Planck constants.

$$\begin{cases} \dfrac{\partial\rho}{\partial t}+\dfrac{\partial(\rho u)}{\partial x}+\dfrac{\partial(\rho v)}{\partial y}+\dfrac{\partial(\rho w)}{\partial z}=0 \\ \dfrac{\partial(\rho u)}{\partial t}+\mathrm{div}(\rho uu)=-\dfrac{\partial p}{\partial x}+\dfrac{\partial\tau_{xx}}{\partial x}+\dfrac{\partial\tau_{xy}}{\partial y}+\dfrac{\partial\tau_{zx}}{\partial z}+F_x \\ \dfrac{\partial(\rho v)}{\partial t}+\mathrm{div}(\rho vu)=-\dfrac{\partial p}{\partial y}+\dfrac{\partial\tau_{xy}}{\partial x}+\dfrac{\partial\tau_{yy}}{\partial y}+\dfrac{\partial\tau_{zy}}{\partial z}+F_y \\ \dfrac{\partial(\rho w)}{\partial t}+\mathrm{div}(\rho wu)=-\dfrac{\partial p}{\partial z}+\dfrac{\partial\tau_{xz}}{\partial x}+\dfrac{\partial\tau_{yz}}{\partial y}+\dfrac{\partial\tau_{zz}}{\partial z}+F_z \\ \dfrac{\partial(\rho T)}{\partial T}+\mathrm{div}(\rho uT)=\mathrm{div}\left(\dfrac{K}{c_p}\mathrm{grad}T\right)+S_T \end{cases} \tag{4}$$

where ρ denotes the fluid density (kg/m^3), t is time (s); *u, v,* and *w* represent the velocity components in the *x, y,* and *z* directions, respectively (m/s); and *p* is the pressure on the fluid micrometabolite (Pa); τ_{xx}, τ_{xy} and τ_{xz} denote the three components of the fluid internal stress tensor τ along the *x, y* and *z* directions at the surface of the micrometabolite due to the presence of intermolecular viscous forces; F_x, F_y and F_z are the micrometric volumetric force per unit mass of fluid (N); *T* is the fluid temperature (K); c_p is the specific heat capacity (J/(kg·K)); *K* indicates the fluid heat transfer coefficient (W/m^2·K) and S_T is the fluid heat source.

A three-dimensional physical model of the thermal insulation space is established as shown in Fig. 4, with main structural dimensions presented in Tab. 2.

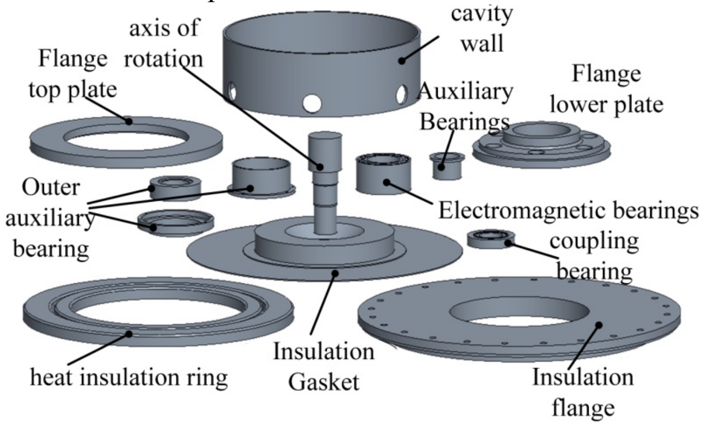

Fig. 3 Three-dimensional physical modeling of insulated spaces.

Tab. 2 Main structural parameters

Main structure	Inside radius (mm)	Outside radius (mm)	Number of holes	Radius of holes (mm)
Cavity wall	745	760	6	75
Flange	225	745	6	65
Inner heat-Insulation ring	670	800	--	--
Outer heat-Insulation ring	830	1050	--	--
Insulation flange	540	1250	--	--
Insulation gasket	185	1070	--	--

Fig. 5 (a) shows the simplified model of the insulated space, and Fig. 5 (b) displays the 1/6 mesh division of this simplified model. The fluid and solid domains used to solve the model are highlighted in the figure. As demonstrated in Fig. 6, grid independence was verified to ensure that the results do not vary with the number of grids used in the study, all meeting calculation requirements. The maximum temperature values for sections b, c, and d are included in the figure, with the section positions detailed in Fig. 8 of Section 2.3.1. For the calculations, helium is specified as the fluid material, insulation cotton as the material for the insulation ring, and steel for other structures.

To accurately solve the thermal insulation space model and calculate the fluid and temperature fields, the basic assumptions and boundary conditions of the solution domain are outlined as follows:

1) As indicated by Tab. 1, with a Reynolds number greater than 10,000, the model exhibits turbulent flow within the calculation area.
2) Helium is considered an incompressible fluid and treated as steady-flowing.
3) The inlet location is defined as a velocity inlet boundary condition in Fig. 5(b), with an inlet flow rate of 11.80 m^3/s and wind speed of 8 m/s, as provided by the fluid network results.
4) The outlet location is specified as a pressure outlet boundary condition with an ambient pressure of 1 standard atmosphere in Fig. 5(b).
5) The insulated space is subjected to multiple heat sources and a high-temperature gradient environment. Considering the operating condition of the drive motor, a low-temperature heat source of 60℃ is located at the inlet surface, while the high-temperature heat source is within the fan cavity basin, set at 250℃.

6) No-slip boundary conditions are assumed for the fluid-solid contact surfaces within the solution domain.

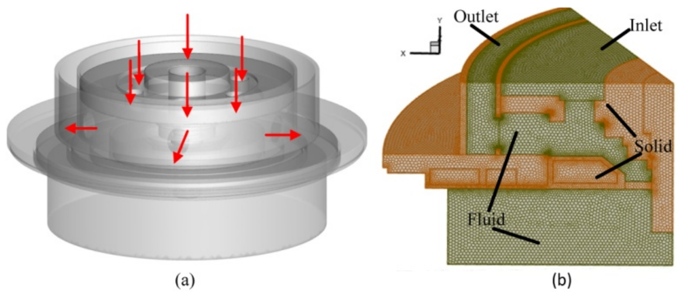

Fig. 5 Three dimensional simplified model of thermal insulation space and solution domain mesh.
(a) Simplified model. (b) Solution domain and mesh.

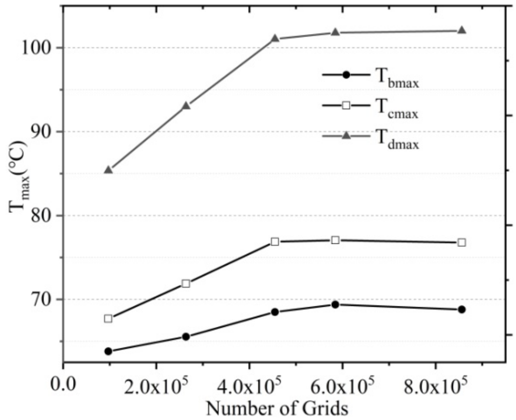

Fig. 6 Results of grid dependence test.

2.3. Fluid field and temperature field calculation and analysis

2.3.1 Calculation and analysis of fluid fields in insulated spaces

Based on fluid mechanics calculation equations, the fluid distribution in the insulation space was obtained. Figure 7 illustrates the flow field velocity cloud and trace distribution within the basin of the insulated space. It is evident from the graph that helium enters from the inlet and reaches a maximum speed of 233.7 m/s at the halfway-through hole. As the fluid flow paths are dispersed, the fluid interactions in each path make the flow state of helium gas complex, forming vortices at positions 1 and 2 in the figure and reducing the flow velocity.

To thoroughly analyze the distribution of fluid and temperature fields, cross-sections a (Y=-0.10m), b (Y=-0.15m), c (Y=-0.20m), d (Y=-0.25m), e (Y=-0.30m), and f have been delineated. Cross-sections a, b, and c represent the fluid domain cross-sections, while d and e represent the solid domain, as illustrated in Fig. 8.

Fig. 9 displays the flow velocity distribution for axial data collection at section b, where the maximum flow velocity occurs at 179.28 m/s directly below the through-hole. Due to the large variation in fluid velocity, a vortex was formed at location 1. Meanwhile, influenced by the wall structure, vortices are formed at locations 2 and 3. Vortex changes the fluid flow state, causing a decrease in flow velocity.

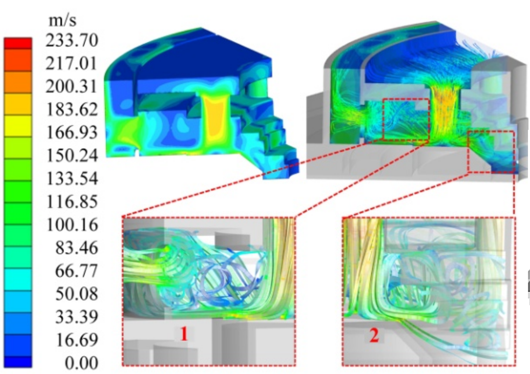

Fig. 7 Insulated space flow field maps and traces.

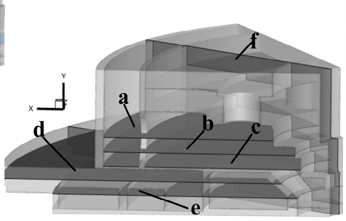

Fig. 8 Data cross sections.

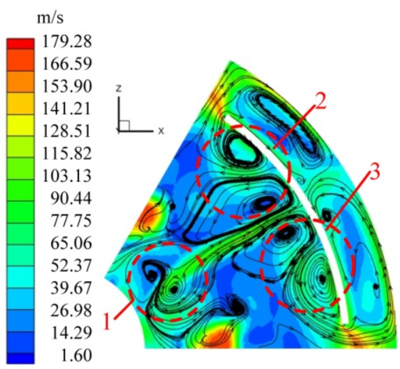

Fig. 9 Flow velocity distribution at section b.

2.3.2 Calculation and analysis of temperature field in insulated spaces

Due to the special working environment of insulated spaces, there is thermal conduction between solids in the insulated space. Helium gas undergoes convective heat transfer with solids during the flow process, and solids undergo thermal radiation when heated at high temperatures in the insulated space. This article considers three heat transfer modes: heat conduction, heat convection, and heat radiation during the calculation. Based on the heat transfer control Eq. (5), the temperature field of the insulated space was solved.

$$\begin{cases} \dfrac{\partial}{\partial x}\left(\lambda_x \dfrac{\partial T}{\partial x}\right) + \dfrac{\partial}{\partial y}\left(\lambda_y \dfrac{\partial T}{\partial n}\right) + \dfrac{\partial}{\partial z}\left(\lambda_z \dfrac{\partial T}{\partial z}\right) = -q_V \\ T\big|_{S_1} = T_0 \\ \lambda \dfrac{\partial T}{\partial n}\bigg|_{S_2} = q_0 \\ \lambda \dfrac{\partial T}{\partial n}\bigg|_{S_3} = -\alpha(T - T_f) \\ \lambda \dfrac{\partial T}{\partial n}\bigg|_{S_4} = -\varepsilon\sigma(T^4 - {T_f}^4) \end{cases} \tag{5}$$

where T denotes the temperature of the boundary surface of the object; q_V indicates the sum of each heat source in the solution domain; λ_x, λ_y and λ_z represent the thermal conductivity coefficients of various materials along the *x, y* and *z* directions, respectively; S_0 is the boundary surface of the thermostat; T_0 is the temperature of the boundary surface of the thermostat; q_1 is the density of the heat flow on the boundary surface S_1; α is the surface heat dissipation coefficient; ε represents the emission coefficient; and σ is the Stefan-Boltzmann constant.

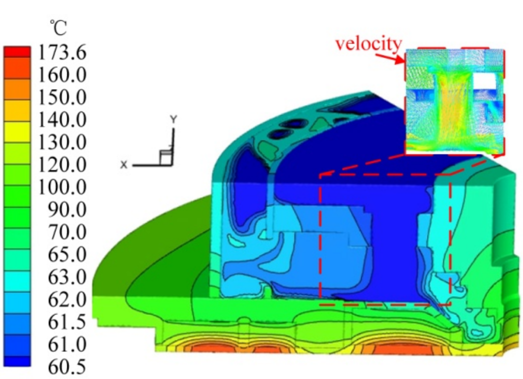

Fig. 10 Insulated space temperature distribution cloud.

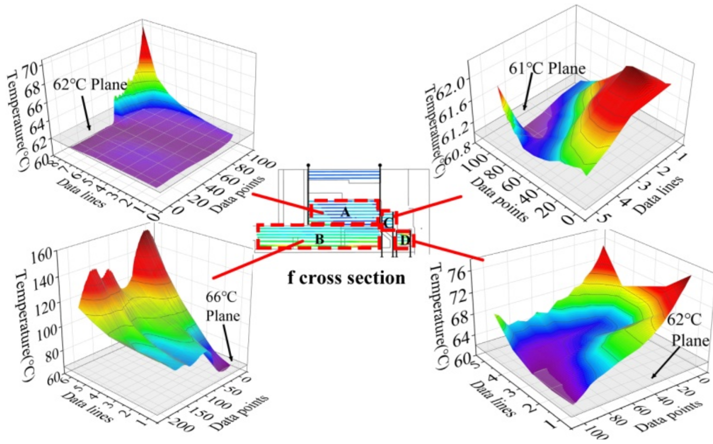

Fig. 11 Temperature distribution along the collecting line in cross section f.

Fig. 10 illustrates the overall temperature field distribution in the insulated space. The space is influenced by the high temperature of helium gas in the fan chamber, with the highest temperature of 173.6□ located at the insulation gasket and flange directly below the insulation ring in the solid domain. As heat transfers upward, the temperature in the solid domain gradually decreases, and the temperature in the helium basin remains generally low. The heat of high-temperature helium gas in the fan chamber decreases significantly after passing through the insulation flange, and the temperature gradient on both sides of the insulation flange is large, which has a significant inhibitory effect on heat transfer. The flow of helium gas through the flange’s through-hole increases the flow rate, enhancing the heat dissipation effect. Consequently, the upper perforated flange serves to enhance and suppress heat transfer. These two key components warrant focused study.

To examine the temperature distribution within the fluid domain of the insulated space in detail, cross-section f, as shown in Fig. 8, is analyzed. This section is divided into four zones: A, B, C, and D, where A, C, and D are fluid domains and B is a solid domain. As depicted in Fig. 11, most temperatures in the basins do not exceed 62°C. However, it can be seen that the temperature gradient is obvious, and the temperature difference in zone B can reach a maximum of about 90 □, which is not conducive to the stability and sealing of the large flange.

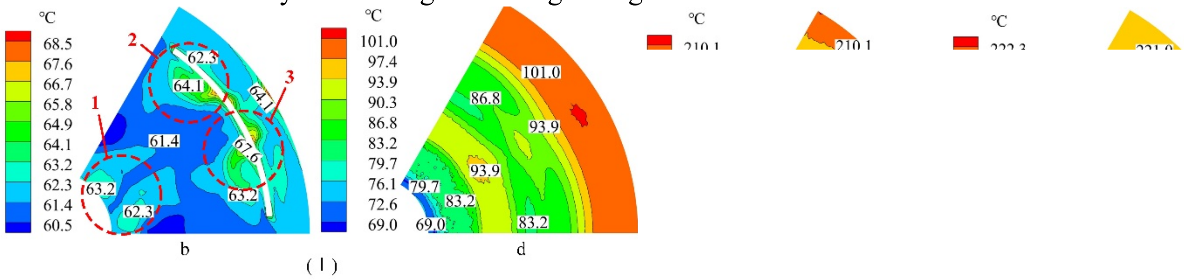

Fig. 12 Cross-sectional temperature clouds for two heat transfer cases.

(I) With forced convection heat transfer. (II) No forced convection heat transfer.

In order to study the heat transfer characteristics of insulated space, this paper controls different heat transfer equations to explore the primary and secondary effects of heat transfer modes on the heat insulation capacity of insulated space. This article calculates the temperature field of an insulated space without forced convection heat transfer. A comparative analysis was conducted between the temperature field without forced convection and the temperature field with forced convection (normal operation of insulated spaces) mentioned earlier.

As shown in Fig. 12, Scenario (I) for the case with forced convection (normal operation of insulated spaces), the maximum temperature of section b is 68.5°C, and the maximum temperature of section d is 101°C; Scenario (II), where forced convection heat transfer is absent, generally shows higher temperatures across the sections. Tab. 4 displays a comparison of the maximum and average temperatures across the five cross-sections for the two heat transfer scenarios. It can be seen that forced convection causes a decrease in the overall temperature of the insulation space. In addition, Fig. 12-(I) corresponds to positions 1, 2, and 3 indicated in Fig. 9. It can be seen that the fluid forms vortices due to changes in flow velocity and the influence of wall surfaces. The vortices not only change the fluid flow state, causing a decrease in flow velocity, but also lead to energy accumulation, resulting in higher temperatures and poorer heat dissipation effects, indicating that these areas are unfavorable vortices.

Tab. 3 Comparison of cross-section temperatures for two heat transfer cases.

		a	b	c	d	e
T_{max}(□)	□	67.2	68.5	76.4	101.5	127.1
	□	205.3	210.1	217.3	222.3	225.5
T_{ave}(□)	□	61.8	62.0	62.3	91.7	110.1
	□	188.8	199.2	210.5	219.5	223.3

Combining Fig. 12 and Tab. 3, it can be seen that the temperature gradient in the insulated space without forced convection is small, and the overall temperature is generally very high; the insulation space with forced convection participation has a large temperature gradient, and through forced convection heat transfer, the temperature of the insulation flange drops significantly, which has a good thermal suppression effect. Comparing the simulation results of two heat transfer scenarios, it was found that thermal convection played an effective role in suppressing heat transfer from high-temperature helium gas to the working chamber.

In conclusion, both thermal insulation materials and convective heat transfer play significant roles in suppressing heat transfer. Enhancing the thermal suppression behavior of the insulated space can be achieved by improving either aspect. Considering that improving the performance of insulation materials may further cause uneven temperature distribution of insulation flanges, targeted optimization strategies for spatial structures can be proposed by enhancing convective heat transfer in the future.

2.4. Experimental validation of insulation space temperature calculation results

Through the analysis of fluid and temperature fields in the heat-insulating space, we established the temperature distribution law within this space. To verify the accuracy of these calculations, we gathered monitoring data from the insulated space during the operation of the main helium fan test platform.

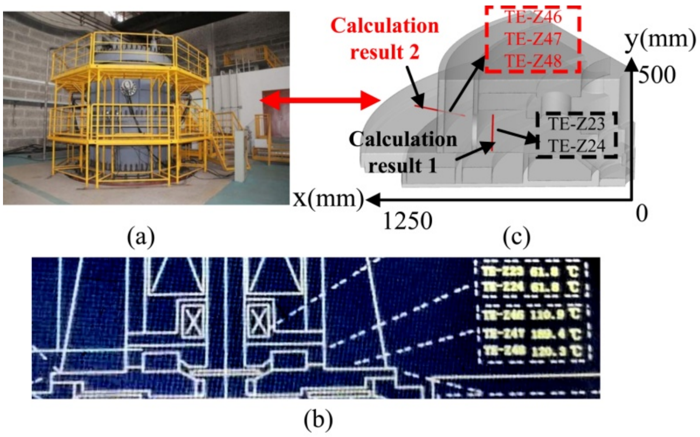

Fig. 13 Main helium fan test platform monitoring. (a)High-temperature gas-cooled reactor nuclear power plant demonstration project test platform. (b) Data acquisition line simulation. (c) Schematic diagram and data results of the experimental platform monitoring.

In Fig. 13(a), the test platform for the demonstration project of a high-temperature gas-cooled reactor nuclear power plant, developed jointly by Huaneng Shandong Shidaowan Plant and Harbin Electric Group Jiamusi Electric Company Limited, is shown. The testing environment replicated the simulation conditions, with the initial temperature of the helium gas in the insulated space set at 60°C and the operating pressure at 0.1 MPa, while ensuring the hermeticity of the experimental helium as the medium. A heater was placed at the bottom of the test platform to simulate a high-temperature heat source of 250°C, mimicking the high-temperature helium gas in the fan chamber. Fig. 13(b) illustrates the schematic of the experimental platform monitoring system, which includes data results, with two temperature measurement units (TE-Z23 and TE-Z24) located in the helium basin of the chamber and three temperature measurement units (TE-Z246, TE-Z47, and TE-Z48) positioned on the insulation flange. Fig. 13(c) displays the schematic diagram of the simulation data acquisition lines, identifying the locations for simulation and test data acquisition, with '1' marking the watershed temperature acquisition line and '2' the insulation flange temperature acquisition line, matching the test monitoring locations. The experimental process is outlined in Fig. 14.

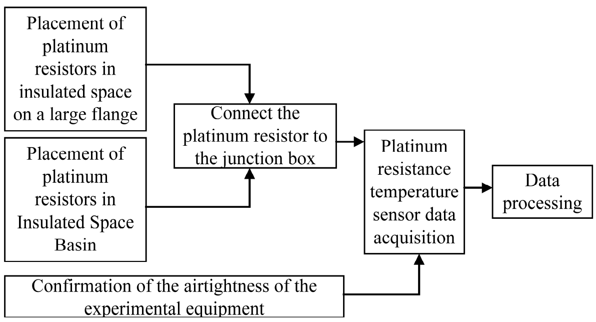

Fig. 14 Experimental flowchart.

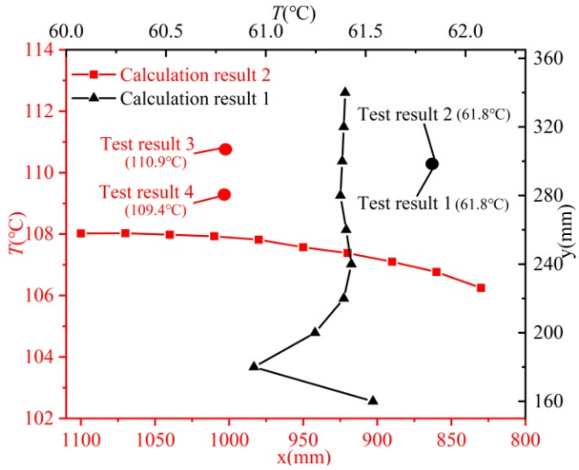

Fig. 15 Comparison of experimental and calculated results.

The test results from the main helium fan test platform led to the exclusion of an interference term with a large error (TE-Z48) from the test results. Fig. 15 shows the comparison between the simulation calculations and the four experimental results obtained through monitoring. The x-axis represents the horizontal direction and the y-axis the vertical direction, aligning with Fig. 13(c). "Test result 1" and "Test result 2" are associated with test points TE-Z23 and TE-Z24, respectively, located at y=300 mm. "Test result 3" and "Test result 4" correspond to test points TE-Z46 and TE-Z247, respectively, located at x=1000mm. The vertical "Calculation result 1" represents the simulation data acquisition line with a length of 200 mm, corresponding to the placement of the platinum resistor in the helium basin of the chamber. The horizontal "Calculation result 2" shows the simulation data acquisition line with a length of 300mm, corresponding to a platinum resistor placed at the heat insulation flange. To minimize errors due to positional deviation, 10 data points were extracted equidistantly along the acquisition line for averaging. The maximum error between the averaged simulation data and the test values was about 2.8%, which falls within the acceptable range for engineering calculations. These results validate the rationality of the simplified model presented in this paper, confirming that the calculations are reliable and providing a solid foundation for further research on thermal insulation space.

3. Space thermal equilibrium determination

To assess the same issue from various viewpoints, this article introduces a measurement coefficient to evaluate the uniformity of temperature distribution using a common benchmark. Additionally, for the thermal balance issue in insulated spaces with high temperature gradients, the concept of temperature deviation triangles and temperature deviation coefficient angles is proposed to assess temperature distribution uniformity.

As illustrated in Fig.16, T_{ave} represents the average temperature of the insulation space; ΔT_{max} is the difference between the maximum temperature T_{max} and the average temperature T_{ave} of the insulation space; ΔT_{min} is the difference between the minimum temperature T_{min} and the average temperature T_{ave}; ΔT_{imax} is the difference between the maximum temperature T_{imax} and the average temperature T_{ave} of the ith axial section, while ΔT_{imin} is the difference between the minimum temperature T_{imin} and the average temperature T_{ave} of the ith axial section. $\theta_{\max}$ is defined as the maximum temperature deviation coefficient angle, $\theta_{\min}$ as the minimum temperature deviation coefficient angle, θ_{imax} as the maximum temperature deviation coefficient angle of the ith axial cross-section, θ_{imin} as the minimum temperature deviation coefficient angle of the ith axial cross-section, and $\Delta\theta$ as the range of the temperature deviation coefficient angle.

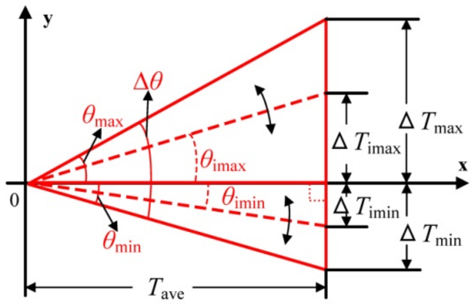

Fig. 16 Temperature deviation triangle.

$$\begin{cases} \theta_{\max} = \arctan\dfrac{T_{\max} - T_{\mathrm{ave}}}{T_{ave}} = \arctan\dfrac{\Delta T_{\max}}{T_{ave}} \\ \theta_{\min} = \arctan\dfrac{T_{\min} - T_{ave}}{T_{ave}} = \arctan\dfrac{\Delta T_{\min}}{T_{ave}} \\ \theta_{\mathrm{imax}} = \arctan\dfrac{T_{\mathrm{imax}} - T_{ave}}{T_{ave}} = \arctan\dfrac{\Delta T_{\mathrm{imax}}}{T_{ave}} \\ \theta_{\mathrm{imin}} = \arctan\dfrac{T_{\mathrm{imin}} - T_{ave}}{T_{ave}} = \arctan\dfrac{\Delta T_{\mathrm{imin}}}{T_{ave}} \end{cases} \tag{6}$$

The relation between the deviation coefficient angle and temperature is presented in Equation (6). From the temperature deviation coefficient angle given in Eq.(6) and the temperature deviation triangle seen in Fig. 16, it is evident that a smaller θ deviation coefficient angle indicates that the helium basin temperature is closer to the insulation space's average value, signifying a more uniform temperature distribution.

4. Study of factors influencing temperature distribution in insulated spaces

The working pressure in insulated spaces can reach as high as 7 MPa, and changes in pressure significantly affect heat transfer [14]. Consequently, understanding the thermal distribution in insulated spaces requires considering the effects of pressure. The flange through-hole is the sole path for helium to enter the chamber within the insulated space, and its structural design directly influences the fluid flow characteristics and, thus, the thermal distribution in the space. Therefore, this article selects pressure and through-hole structure as variables for studying the temperature distribution and thermal equilibrium performance. Furthermore, since the insulation flange serves as a connecting structure feature in the thermal insulation space, it is noted that the high temperature gradient at the insulation flange, as discussed in section 2.3.2, can generate substantial local stress and potentially lead to structural damage. Thus, the critical cross-section d of the insulation flange, characterized by a high-temperature gradient, is chosen as the focus for research. Observations and analyses emphasize the temperature changes and thermal equilibrium of the cross-section under varying conditions, where thermal equilibrium is determined by the temperature deviation angle coefficient. All calculations are performed using the 3D physical model of the insulated space described in Chapter 2.

4.1. Effect of different pressures on the temperature of an insulated space

To explore how different pressures affect the temperature within an insulated space, we examined eight distinct pressure environments: 0.1 MPa, 0.3 MPa, 0.5 MPa, 0.7 MPa, 1 MPa, 3 MPa, 5 MPa, and 7 MPa. We applied the single-variable method to analyze temperature changes and thermal equilibrium at cross-section d under these varying pressures.

The effect of Fig.17 (a) illustrates the temperature at section d under different pressures, showing that the overall temperature decreases as pressure increases. This decrease occurs because the helium's density per unit volume increases with pressure, enhancing its heat transfer efficiency and dissipative effect, thereby lowering the temperature of the insulated space. This relationship suggests that the impact of pressure on heat transfer is inversely proportional. Additionally, once the pressure reaches a certain level, the helium's density stabilizes, and further increases in pressure do not significantly affect the heat transfer.

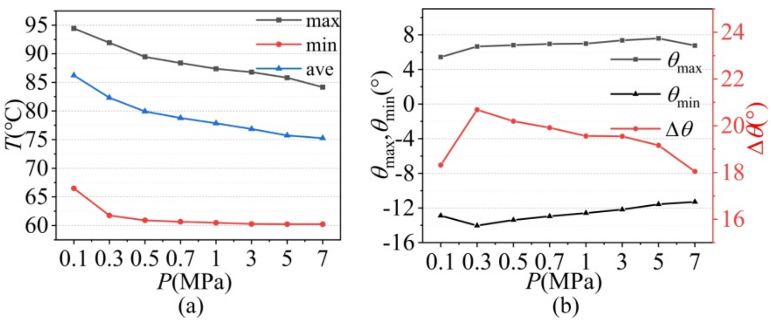

Fig. 17 The variation of *T* and $\Delta\theta$ in cross-section d under different pressures. (a) The variation of *T*. (b) The variation of $\Delta\theta$.

Fig. 17 (b) displays the temperature deviation angle at cross-section d under different pressures. As pressure increases, the deviation angle range $\Delta\theta$ initially increases and then decreases, reaching its minimum of 18.04° at 7 MPa, indicating optimal thermal equilibrium.

4.2. Different through-hole apertures on the temperature of insulated spaces

To assess the impact of aperture sizes on the temperature within an insulated space, we selected five structures with a through-hole radius of 55 mm, 60 mm, 65 mm (original model), 70 mm, and 75 mm to calculate and analyze temperature changes and thermal equilibrium at section d.

Tab. 4 presents the temperatures at cross-section d under various aperture sizes, showing that the maximum and average temperatures initially decrease and then increase as the aperture radius enlarges, while the minimum temperature consistently rises. A smaller aperture restricts the flow path, resulting in a higher helium flow rate, less efficient heat transfer, and higher temperatures at the cross-section. Conversely, a larger aperture increases the flow path's cross-sectional area, reducing helium flow velocity, the Nusselt number, and the heat transfer coefficient, thus elevating the temperature. Fig. 18 (a) demonstrates that with the enlargement of aperture size, the temperature deviation angle $\Delta\theta$ gradually decreases, suggesting an improvement in thermal equilibrium.

Tab. 4 Section d temperature under different aperture sizes

R(mm)	T_{max} (□)	T_{min} (□)	T_{ave} (□)
55	95.97	65.55	87.23
60	96.04	66.17	87.56
65	94.43	66.50	86.23
70	95.83	67.38	87.90
75	96.03	67.54	88.26

4.3. Effect of different numbers of through-holes on the temperature of insulated spaces

To investigate how the number of through-holes in the flange plate influences the temperature within an insulated space, we varied the number of holes while maintaining a constant radius of 65 mm, based on the original model's structure. We analyzed temperature changes and thermal equilibrium at section d with 2, 4, 8, and 10 holes.

Tab. 5 displays the temperature of cross-section d under varying numbers of holes, showing that the maximum temperature value initially decreases and then increases with an increase in the number of holes, while the average and minimum temperatures gradually rise. The alteration in the number of holes indirectly changes the cross-sectional size of the flow path and also modifies the fluid flow path, which means the number of holes and the pore size each uniquely affect the temperature changes. Fig. 18 (b) illustrates that with an increase in the number of holes, the temperature deviation angle $\Delta\theta$ gradually decreases, indicating an improvement in thermal equilibrium.

Tab. 5 Section d deviation angle at different hole numbers

Number of holes	T_{max} (□)	T_{min} (□)	T_{ave} (□)
2	96.54	61.37	85.56
4	95.31	62.99	85.58
6	94.43	66.50	86.23
8	95.11	68.37	87.55
10	96.64	76.73	89.48

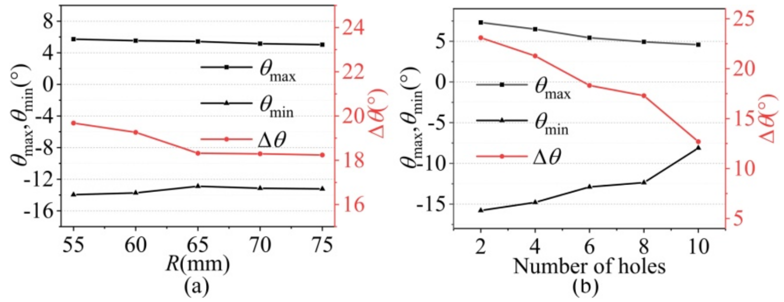

Fig. 18 Changes in Δθ at the section d under different conditions.

(a) Different apertures. (b) Different number of holes.

5. Response surface-based optimization of through-hole structures

Following the analysis of factors affecting temperature distribution in the insulated space, this paper employs the Response Surface Method (RSM) **Error! Reference source not found.** to analyze the highest temperature and thermal equilibrium response variables at cross-section d, with pore size and number of holes as variables, to determine the optimal through-hole structure.

Tab. 6 The CCD Design Matrix

Run	A	B	$\Delta\theta$ (°)	T_{max} (℃)
1	6	75	18.24	96.03
2	2	65	23.10	96.54
3	6	55	19.68	95.97
4	6	65	18.32	94.43
5	6	65	18.32	94.43
6	8	70	16.16	92.97
7	6	65	18.32	94.43
8	4	60	19.55	91.99
9	8	60	17.29	93.04

10	4	70	18.68	92.15
11	10	65	12.69	96.64

Tab. 6 details the $T_{\max}$ and $\Delta\theta$ responses for different pore sizes and hole counts, where A represents the number of holes and B the radius of the hole.

Additionally, the second-order regression equations for the response are shown in equations (7) and (8).

$$\Delta\theta = 18.13\text{-}2.13 \times A\text{-}0.4061 \times B\text{-}0.0624 \times AB\text{-}0.0949 \times A^2 + 0.1719 \times B^2 \quad (7)$$

$$T_{\max} = 93.24 + 0.1742 \times A + 0.0185 \times B\text{-}0.0559 \times AB + 0.6146 \times A^2 + 0.04669 \times B^2 \quad (8)$$

Fig. 19 illustrates the $\Delta\theta$ and $T_{\max}$ response surface models, and the optimization objectives are further analyzed by combining the response surface results. When the number of holes is 7 and the hole radius is 66 mm, the minimum value of $T_{\max}$ is 93.68°C, and the minimum value of $\Delta\theta$ reaches 16.50°.

Fig. 20 displays the flow velocity distribution in the optimized cross-section b. The figures reveal that the situation of eddy currents has also improved post-optimization compared to what is shown in Fig. 9.

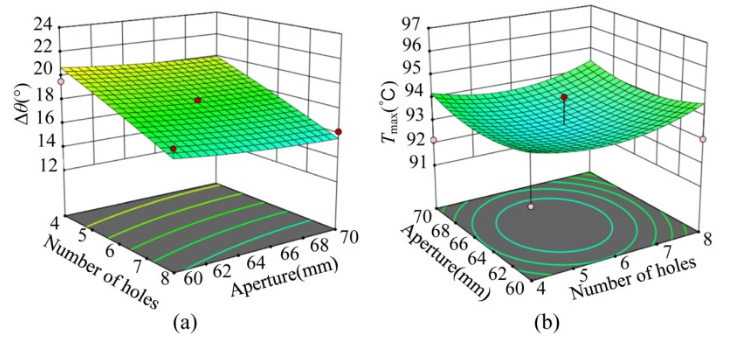

Fig. 19 Response surface model of cross-section d. (a) $\Delta\theta$ response surface model. (b) $T_{\max}$ response surface model.

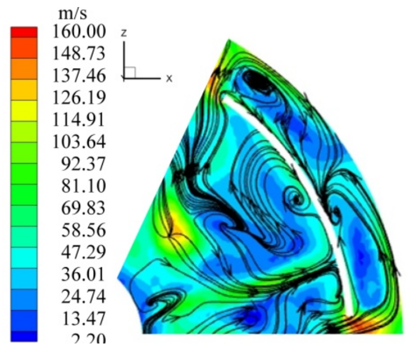

Fig. 20 Optimized flow velocity distribution in the rear section b.

Tab. 7 compares the results of the original model, the predicted model, and the actual model. The percentage errors of the responses $T_{\max}$ and $\Delta\theta$ were 3.20% and 0.86%, respectively, well within acceptable limits. The comparison demonstrates that after optimization, the maximum temperature decreases by 4.00% and the deviation angle range by 9.12%, signifying enhanced thermal suppression and balance in the insulated space.

Tab. 7 Validation test of RSM optimize results

Response	Original	Predicted	Actual	%Error	%Optimization
$T_{\max}$ (℃)	94.43	93.68	90.66	3.20	4.00(↓)
$\Delta\theta$ (°)	18.32	16.50	16.65	0.86	9.12(↓)

6. Conclusion

In this paper, we have studied the thermal inhibition behavior and influencing factors of the thermal insulation space in high-temperature gas-cooled reactors. The following conclusions have been drawn:

(1) We utilized a combination of fluid network and flow-heat coupling models to study the flow-heat dynamics and thermal suppression behavior of the thermal insulation space. The three heat transfer modes of heat conduction, heat convection, and heat radiation coexist in an insulated space. During the heat transfer process, the key structural components of the insulated space, such as the insulation flange and forced convection heat transfer, can all play a role in heat suppression. The temperature results from both calculation and experiment show an error of less than 3%, validating the effectiveness of the simplified model of the thermal insulation space. These findings not only provide a theoretical basis for the application of thermal insulation in engineering but also lay the groundwork for enhancing the operational functionality of these spaces.

(2) This article proposes a method for determining thermal equilibrium parameters based on the spatial relationship of temperature parameters, which improves the comparative efficiency of temperature distribution in insulation spaces. By examining the nonlinear mapping relationship between environmental variables, structural parameters, and judgment parameters, it was observed that at the critical flange section d, higher ambient pressure corresponds to lower temperatures. The optimal thermal equilibrium performance was noted at an angular coefficient of deviation of 18.04°at 7 MPa. Additionally, variations in the number and size of holes significantly impact both the temperature and thermal equilibrium of the insulation space. These findings offer guidance for optimizing thermal insulation spaces, and the thermal parameter evaluation method is broadly applicable across various engineering fields.

(3) Through the application of the response surface method, the optimal configuration was found to include 7 through-holes with a radius of 66 mm each. Post-optimization, the maximum temperature in the watershed of the thermal insulation space decreased by 4.00%, and the range of deviation angles was reduced by 9.12%. The errors between the optimization results and finite element results were within acceptable limits. Structural optimization enhanced the thermal suppression capabilities of the insulated space, effectively improving the helium vortex situation in the previous cavity and strengthening both thermal balance and the overall thermal suppression function of the insulation space. This, in turn, improves the service capability of the drive motor.

References

[1] Yalew,S.G., et al., Impacts of Climate Change on Energy Systems in Global and Regional Scenarios, Nature Energy, 5 (2020), 10, pp. 794-802

[2] Kabeyi,M.J.B., Olanrewaju,O.A., Sustainable Energy Transition for Renewable and Low - Carbon Grid Electricity Generation and Supply, Frontiers in Energy Research, 9 (2022)

[3] Mo,F., Zhang,Y., Wang,H., HTR - PM Main Helium Fan Motor Cooling Performance Analysis, Journal of Tsinghua University(Science and Technology), 58 (2018), 2, pp. 188 - 191

[4] Zou,D., Technical Overview of Main Helium Fans for High - Temperature Gas - Cooled Reactor Nuclear Power Plant Demonstration Project, Explosion - Proof Electric Machine, 4 (2011), pp. 46

[5] Yu,L., et al., Efficient Optimization of Parallel Micro - channel Heat Sinks Based on Flow Resistance Network Model, Applied Thermal Engineering, 233 (2023)

[6] Han,J., Ge,B., Tao,D., Li,W., Influence of Cooling Fluid Parameter on the Fluid Flow and End Part Temperature in End Region of a Large Turbogenerator, IEEE Transactions on Energy Conversion, 31 (2016), 2, pp. 466 - 476

[7] Han,J., Jiechen,D., Wang,Y., Wang,C., Ge,B., Li,W., Coupled Electromagnetic - Fluid - Thermal Analysis for End Zone With Electric Screen in Large Water - Hydrogen - Hydrogen Cooled Turbine Generator Under Different End Winding Extensions, IEEE Transactions on Energy Conversion, 36 (2021), 4, pp. 2703 - 2713

[8] Saxena,G., Singh,D., Raaj,M., Thermal Analysis of a Microhotplate - An Experimental Study. Journal of Microelectromechanical Systems, 29 (2020), 3, pp. 408 - 417

[9] Moussaoui,M. Amine, Derfoufi,S., Mezrhab,A., Fontaine,J., Pierre. Surface Radiation and Natural Convection from Discrete Bottom Heating in Square Cavity. Journal of Thermophysics and Heat Transfer, 36 (2022), 2, pp. 455 - 465

[10] Behera,B. Ranjan, Chandrakar,V., Senapati,J. R., Numerical analysis of combined free convection and radiation heat transfer from an open hemispherical cavity. Numerical Heat Transfer, Part A: Applications, 84 (2023), 9, pp. 1014 - 1031

[11] Karadağ, R., New approach relevant to total heat transfer coefficient including the effect of radiation and convection at the ceiling in a cooled ceiling room. Applied Thermal Engineering, 29 (2009), 8 - 9, pp. 1561 - 1565

[12] Saravanan,S., Sivaraj,C., Coupled thermal radiation and natural convection heat transfer in a cavity with a heated plate inside. International Journal of Heat and Fluid Flow, 40 (2013), pp. 54 - 64

[13] Mezrhab,A., Bouali,H., Amaoui,H., Bouzidi,M., Computation of combined natural - convection and radiation heat - transfer in a cavity having a square body at its center. Applied Energy, 83 (2006), 9, pp. 1004 – 1023

[14] Xu, X., Ge, B., Tao, D., Han, J., Wang, L., Effect of helium on temperature rise of helium blower drive motor in high - temperature gas - cooled reactor. Applied Thermal Engineering, 159 (2019)

[15] Haider, J. A., Ahammad, N. A., Khan, M. N., et al., Insight into the study of natural convection heat transfer mechanisms in a square cavity via finite volume method, International Journal of Modern Physics B, 37 (2023), 04, pp. 2350038.

[16] Khatamifar, M., Lin, W., Dong, L., Transient conjugate natural convection heat transfer in a differentially - heated square cavity with a partition of finite thickness and thermal conductivity, Case Studies in Thermal Engineering, 25 (2021), 100952.

[17] Zhou,D., et al., A Parametric Study of Thermal Stress and Analysis of Creep Strain Under Thermal Cyclic Loading in a Hybrid Quad Flat Package. IEEE Transactions on Components, Packaging and Manufacturing Technology, 11 (2021), 3, pp. 435 - 443

[18] Gu,Y., Wang,X., Gao,P., Li,X., Mechanical Analysis With Thermal Effects for High - Speed Permanent - Magnet Synchronous Machines. IEEE Transactions on Industry Applications, 57 (2021), 5, pp. 4646 - 4656

[19] Yang,X., Guo,J., Yang,B., Cheng,H., Wei,P., He,Y.-L., Design of non - uniformly distributed annular fins for a shell - and - tube thermal energy storage unit. Applied Energy, 279 (2020)

[20] Gu, Y., Wang, X., Gao, P., & Li, X., Mechanical Analysis With Thermal Effects for High - Speed Permanent - Magnet Synchronous Machines. IEEE Transactions on Industry Applications, 57 (2021), 5, pp. 4646 - 4656

[21] Yang, X.-L., Liu, M.-Y., Song, H., Rao, J., Wu, Y.-H., Optimization and Invasive Monitoring for the Local Flow Velocity Maldistribution in Plate - Fin Heat Exchangers. IEEE Transactions on Instrumentation and Measurement, 72 (2023), pp. 1 - 10

[22] Wang, C., Hou, B., Shi, J., Yang, J., Uniformity Evaluation of Temperature Field in an Oven Based on Image Processing. IEEE Access, 8 (2020), pp. 10243 - 10253

[23] Liu, Y., Lin, Y., Wu, K., Fan, H., Wang, L., Analysis and Optimization on Non - uniformity of Temperature Distribution in Hydrophobic Cycloaliphatic Epoxy Resin Insulators during the Curing Process. IEEE Transactions on Dielectrics and Electrical Insulation, 28 (2021), 5, pp. 1810 - 1818

[24] Pang, L., Zhao, N., Xu, H., Li, Z., Zheng, H., Yang, R., Numerical simulations on effect of cooling hole diameter on the outlet temperature distribution for a gas turbine combustor. Applied Thermal Engineering, 234 (2023)

[25] Liang, D., et al., Simplified 3 - D Hybrid Analytical Modelling of Magnet Temperature Distribution for Surface - mounted PMSM With Segmented Magnets. IEEE Transactions on Industry Applications, 58 (2022), 4, pp. 4474 - 4487

[26] Kim, W.-H., Kim, C.-W., Shin, H.-S., Jeong, S.-S., Choi, J.-Y., Optimal Design of Short - Stroke Linear Oscillating Actuator for Minimization of Side Force Using Response Surface Methodology. IEEE Transactions on Magnetics, 58 (2022), 2, pp. 1 - 5

Paper submitted: 05.01.2025
Paper revised: 03.03.2025
Paper accepted: 11.03.2025